CHAPTER II

EXPERIMENTAL APPARATUS

Introduction

The apparatus described here was originally constructed and continues to be used for the study of van der Waals and hydrogen bonded clusters.[1] The detection of IVR induced rovibrational state mixing in jet cooled hydrocarbons presents a different, indeed complementary, set of challenges. For the IVR studies in which the primary experimental challenge is the observation of closely spaced spectral transitions, the instrument's high resolution (10^{-3} cm^{-1}) is a primary advantage. Coupling of the vibrational state which carries oscillator strength to the bath of combination and overtone states produces a spectrum in which the intrinsically overlapping J/K rotational structure is further complicated by the addition of fine structure from the coupled vibrations. The combination of heterogeneous rotational structure and homogeneous vibrational mixing structure can easily produce transitions spaced by <0.005 cm^{-1} (see Chaps. III-VI), making the high resolution of this instrument indispensable. The study of larger van der Waals

clusters, such as Ar_2HF with rotational constants of <0.1 cm^{-1}, also requires excellent spectral resolution merely to observe the closely spaced rotational fine structure (see Chap. VII).

Since van der Waals molecules are weakly bound and exist in at best low concentrations in supersonic expansions, the high sensitivity of the instrument (10^{-4} absorption per pulse in 5 kHz bandwidth (BW)) is a significant advantage for many of these studies. Since the hydrocarbons investigated in the IVR experiments are commercially available, stable molecules, this high detection sensitivity may at first appear to be of little importance for these studies. However, the concentration of the hydrocarbon in the expansion cannot be increased beyond ~2% without the formation of clusters, which further congest the spectrum. Furthermore, since the vibrational state mixing conserves total absorption intensity, the mixing of a single bright state with many dark states will not only split a transition, but also reduce its peak intensity. For example if a bright state mixes equally with 9 other states, 10 transitions will be observed, each ~1/10 the intensity of the unperturbed vibration. In this way, the peak absorption intensity for any individual rovibrational transition and thus the signal to noise ratio can be significantly degraded.

Thus the <u>combination</u> of high resolution and high

detection sensitivity are necessary to pursue successfully the IVR studies as well as those of weakly bound molecules. This Chapter discusses the slit jet, difference frequency, IR laser spectrometer (see Fig. 2.1) which achieves this combination of properties. The spectrometer will be considered in four parts: 1) the generation and tuning of the difference frequency light, 2) the slit jet expansion, 3) the absorption detection and signal acquisition system and 4) the wavelength calibration and data analysis methods.

Difference Frequency Laser System

The use of nonlinear optical, frequency mixing techniques to produce otherwise unavailable laser radiation is quite common in fields employing pulsed lasers; it is somewhat less pedestrian in continuous wave (cw) applications. This fact arises largely from the dependence of the output power upon the square of the input laser's power in processes such as frequency doubling or in the case of difference frequency mixing upon the product of the input lasers' powers. Thus if one starts with a cw laser with a power of 0.5 W instead of a pulsed laser with peak power of easily over 100 KW, the cw system will produce only one ten billionth of the power produced in the pulsed system, all other parameters being equal.

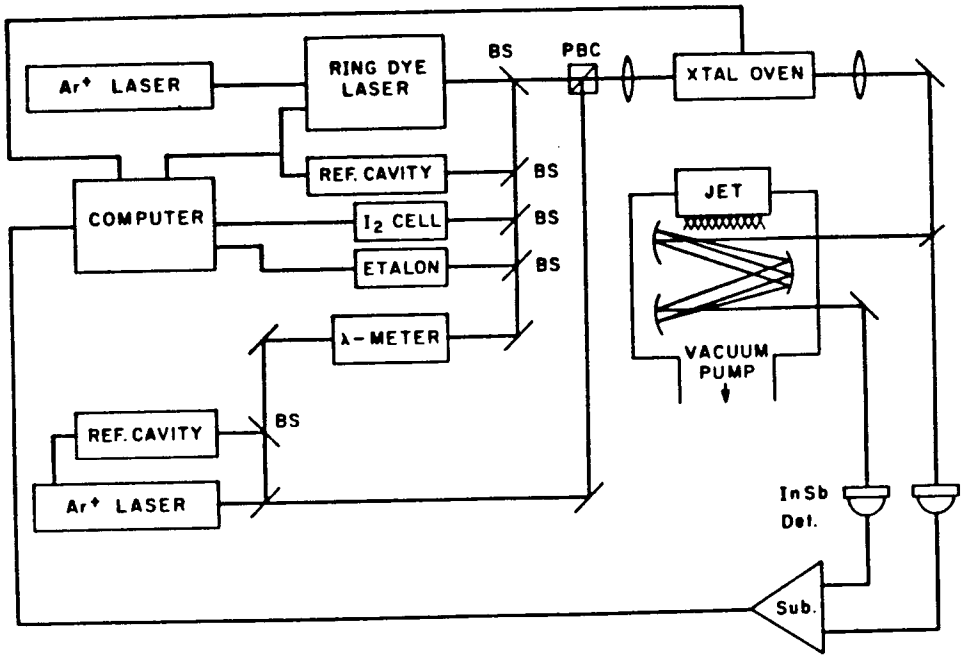

Figure 2.1 Slit jet, difference frequency IR laser spectrometer for 2.2-4.2 μm studies. PBC is a polarization beam splitter used to combine the orthogonally polarized dye and Ar ion lasers. BS is a beam splitter.

However, for some applications laser powers of only a few microwatts are sufficient to achieve quite impressive scientific results. In particular the IR direct absorption apparatus described here requires only a few microwatts of IR laser power to achieve very high sensitivity (10^{-4} absorbance (abs.) in 5 kHz BW). The advantage of low power, cw lasers lies in their narrow band light (10^{-4} cm^{-1} rms frequency noise), a basic necessity for high resolution spectroscopy. Though cw color center lasers also provide very narrow band, tunable light in this region and at much higher powers (up to 500 mW), their frequency coverage is at present relatively limited (2.2-3.2 and 1.4-1.7 μm) compared to that available by difference frequency mixing (1.2-4.2 μm in $LiNbO_3$).

Here a brief review of the physics of difference frequency mixing will be presented; more elaborate presentations are to be found in Refs. 2 and 3. In difference frequency generation, the desired frequency ω_3 is produced by subtracting two higher frequencies ω_1, ω_2,

$$\omega_3 = \omega_1 - \omega_2. \qquad (2.1)$$

The difference frequency ω_3 may also be described as the beat frequency between ω_1 and ω_2.

To produce ω_3, a material with a nonzero second order susceptibility is required. In other words, the second order term, d_{ijk}, in the power series expansion of

electric polarization **P** in terms of the electric field **E**

$$P_i = n_{ij}E_j + d_{ijk}E_jE_k \qquad (2.2)$$

must not vanish (**n** is the index of refraction tensor). The d_{ijk} are nonzero only in media lacking an inversion center. If the vector and tensor nature of **E** and d_{ijk} respectively are temporarily neglected, it is easy to see that this second order term leads to the generation of the difference and sum frequencies. To demonstrate this, we assume two sinusoidally varying electric fields with frequencies ω_1 and ω_2 and amplitudes a_1 and a_2 are incident on a transparent media with an effective second order susceptibility d_{eff}. The product of the electric fields then gives

$$d_{eff}a_1\cos(\omega_1 t)\, a_2\cos(\omega_2 t) = d_{eff}a_1a_2[\cos((\omega_1-\omega_2)t) + \cos((\omega_1+\omega_2)t)] \qquad (2.3)$$

Thus d_{eff} can produce both the sum, $\omega_1+\omega_2$, and difference, $\omega_1-\omega_2$, frequencies. Clearly if $\omega_1=\omega_2$, this is the case of second harmonic generation.

However, more than a nonvanishing second order susceptibility is required for the generation of significant difference frequency light. Just as Eq. 2.1 is a statement of energy conservation, the photon momentum, $n\omega$, must also be conserved

$$n(\omega_3)\omega_3 = n(\omega_1)\omega_1 - n(\omega_2)\omega_2 \qquad (2.4)$$

where $n(\omega_i)$ is the index of refraction at ω_i. This is the

so called phase matching condition. Since the ω_i are fixed by energy conservation, Eq. 2.4 must be satisfied by adjusting $n(\omega_i)$. For example, this can be achieved with a birefringent material, one whose $n(\omega_i)$ along one axis (the extraordinary axis, n_e) is different from that along the other two (the ordinary axes, n_o).

The birefringence is commonly used to satisfy Eq. 2.4 in one of two ways, angle tuning or temperature tuning. If angle tuning is used, ω_1 and ω_2 are linearly polarized with some nonzero angle (usually 90°) between the directions of polarization. To tune $n(\omega_i)$, the nonlinear medium is then rotated by an angle θ measured between the Poynting vector **S** and the optic axis, the direction of n_e. The effective index of refraction sampled by each ω_i is then given by

$$\frac{1}{n_{eff}^2} = \frac{\cos^2\theta}{n_o^2} + \frac{\sin^2\theta}{n_e^2} \qquad (2.5)$$

Fig. 2.2 shows the index ellipsoid which graphically demonstrates the variation of n_{eff} with the angle θ through the medium. Though the angle tuning method can be used with a wide variety of birefringent crystals, it has the disadvantage that the lasers are not in general propagating along a crystal axis and thus are refracted away from each other. The beam overlap and thus coherence length is then quite short. Since the output power in difference frequency mixing depends on the

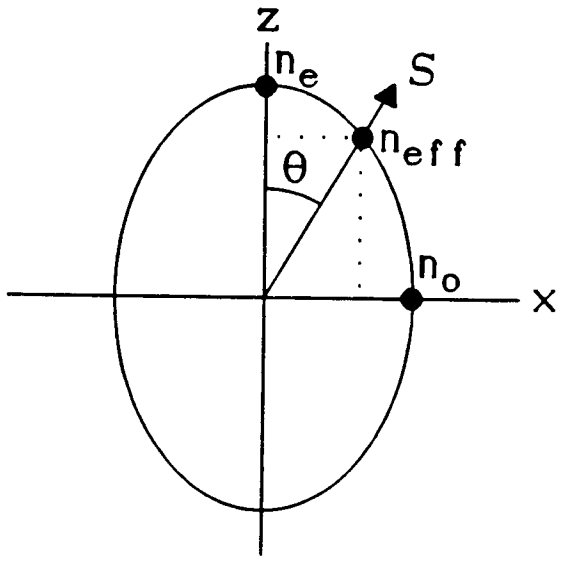

Figure 2.2 The index ellipsoid for a birefringent material showing the effective index of refraction n_{eff} sampled by a laser polarized at an angle θ from the extraordinary axis. The index of refraction along the extraordinary axis is n_e and those along the ordinary axes are n_o.

product of the input powers and the coherence length squared, the beam walk off problem of angle tuning severely limits the conversion efficiency. For pulsed lasers with high peak powers (>100 KW), this is not a catastrophic problem and angle tuning is commonly used. Angle tuning has also been used for cw difference frequency mixing in $LiIO_3$ to produce light between 1.8-5.4 μm at relatively low power levels on the order of 0.1 μW.[4]

However, with low power cw lasers (~500 mW), a long coherence length becomes extremely desirable to maximize the conversion efficiency. This can be obtained if the beams' k-vectors are aligned along the crystal axes, i.e. 90° phase matching, but a different method must then be used to tune $n(\omega_i)$. One method is to make use of the temperature dependence of the indices of refraction. If n_o and n_e have significantly different temperature dependence, heating or cooling the crystal can be used to adjust these indices to satisfy the phase matching condition. $LiNbO_3$ possesses such a large temperature dependence[5] and is transparent from the visible to 4.2 μm[6], making it a suitable material for the difference frequency generation of near IR light.

Difference Frequency Generation of 2.2-4.2 μm Radiation

The difference frequency generation of infrared (IR) light in $LiNbO_3$ by 90° phase-matching using a single

frequency argon ion (0.6 W at 488 or 514 nm, Spectra Physics Model 2020-05) and a ring dye laser (0.4 W with R6G dye, Spectra Physics Model 380A) provides a continuously, tunable high resolution laser source in the near IR from 2.2 to 4.2 μm[7,8]. The IR light produced by this method maintains the excellent amplitude and frequency stability characteristic of the visible pump lasers.

In our implementation of this technique, both visible lasers are frequency stabilized by locking to separate external cavities (Spectra Physics Model 450) with 0.333 cm^{-1} free spectral range (FSR) and finesse of 200. The reference cavities may be electronically scanned over ≤ 3 cm^{-1} (i.e. 9-10 FSR) with a piezo electric transducer (PZT) mounted mirror (0-1 kV). Each laser is locked to the side of a cavity transmission fringe with a home built two stage servo loop circuit shown in Fig. 2.3 which provides both proportional and integrated corrections. A photodiode monitors the frequency dependent transmission of each laser through its reference cavity. When the laser frequency is tuned to coincide with the side of a reference cavity transmission fringe, frequency noise on the laser is converted into a time varying transmission through the cavity as shown in Fig. 2.4. Since amplitude noise on the laser also creates a time varying signal on the photodiode, there is

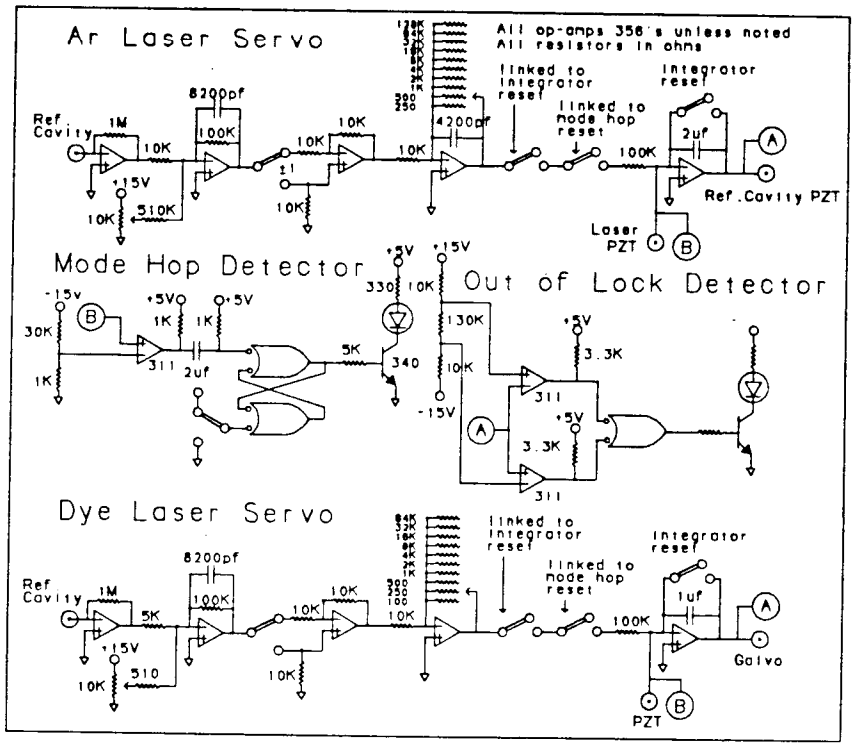

Figure 2.3 Circuit diagrams for the dye laser and Ar ion laser frequency servos.

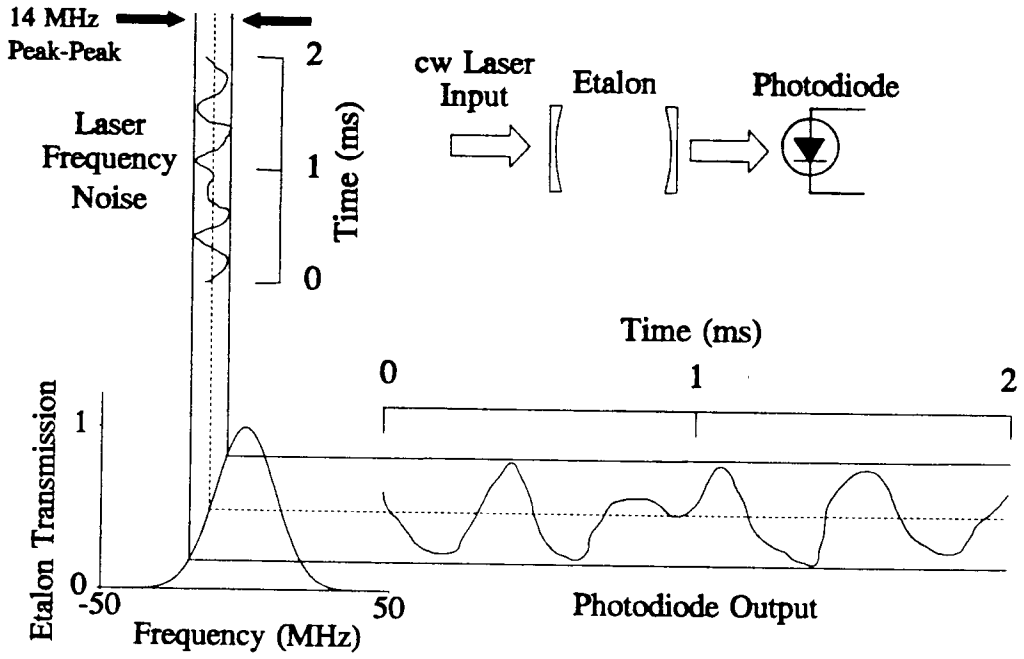

Figure 2.4 Conversion of laser frequency noise into a time varying electronic signal by monitoring transmission through a cavity with laser tuned to the side of a cavity transmission fringe.

the potential for converting amplitude noise to frequency noise, although this has not proven a significant limitation to date. Thus, the photodiode signal from the reference cavity acts as the error signal for the servo circuit.

After amplification in the first stage of the servo circuit, the error signal is a purely negative going voltage. Since we would like zero volts to correspond to no error, this signal is summed with a positive dc voltage to produce a voltage oscillating about ground. In this way, this positive voltage sets the lock point on the cavity fringe. If the voltage exceeds the fringe peak height, the error signal will be always positive and the servo will not lock. A better alternative to summing a dc voltage to the cavity signal is to sum a voltage from a photodiode which measures the laser power. This would have two advantages: 1) it maintains a constant lock point on the fringe as the laser power varies and 2) it reduces the possibility of converting amplitude noise to frequency noise. Though the present system works well, this is a desirable refinement which should be added.

After addition of the offset voltage, the error signal is fed to a variable gain, proportional stage with dc to 2 kHz bandwidth; this controls a PZT mounted, intracavity mirror in each laser to provide correction

for relatively fast frequency noise. By translating these mirrors, the cavity length of the laser is varied, thus tuning the laser frequency and correcting the noise. The bandwidth of this servo system is ultimately determined by PZT mechanical resonances at ~5 kHz.

After the proportional stage, a subsequent integrator stage provides additional correction for slow noise, i.e. drift, occurring on a time scale of seconds to minutes. In the dye laser system, the integrator drives intracavity Brewster plates which are also used to scan the laser. This provides a slow correction with a large dynamic range of up to 3 cm^{-1}. In contrast to the dye laser, the argon laser drifts only 0.010 cm^{-1} over a day due to its intrinsic mechanical stability; this long term stability is much better than that of the reference cavity whose end mirror drifts due to PZT creep. Thus the integrator is used to eliminate drift in the reference cavity while at the same time the proportional output corrects the "fast" noise on the argon laser. The frequency stabilization gives the argon ion and dye lasers, respectively, 1.0 MHz (3×10^{-5} cm^{-1}) and 3 MHz (1.0×10^{-4} cm^{-1}) rms frequency noise in a dc to 2 kHz bandwidth as measured by the additional transmission amplitude noise observed with the laser tuned to the side of a cavity transmission fringe (0.1 cm^{-1} FSR, finesse 200, Spectra Physics Model 450).

The two visible lasers are rendered collinear by using a polarization beam splitter coated to reflect the 514 nm or 488 nm, vertically polarized argon ion laser while transmitting the horizontally polarized dye laser. The beams are then focussed into a 4×4×50 mm $LiNbO_3$ crystal heated to achieve the correct 90° phase matching condition and oriented with the optic axis parallel to the argon ion laser's polarization.[7]

The nickel plated copper oven used to heat the crystal is of commercial design (Chromatix CMX-4/IR) and is used with either the corresponding commercial controller or a home built controller. Both controllers provide temperature stability to 0.05 °C over a 15 min. period in the range 200-500 °C. The circuit diagram for the home built controller is shown in Fig. 2.5. It is essentially identical to the commercial design except for the use of an artificial ice point (Burr-Brown Model SCM5B37/SMXEV) as the thermal couple cold junction compensator. The commercial design uses a resistor network/thermistor compensator, and the oven temperature drifts significantly with the 2-5 °C/day room temperature changes common in the laboratory. These drifts tune the difference frequency phase matching condition by 16-40 cm^{-1}. The home built design is largely immune to this type of long term drift.

Fig. 2.6 shows the phase matching curves for

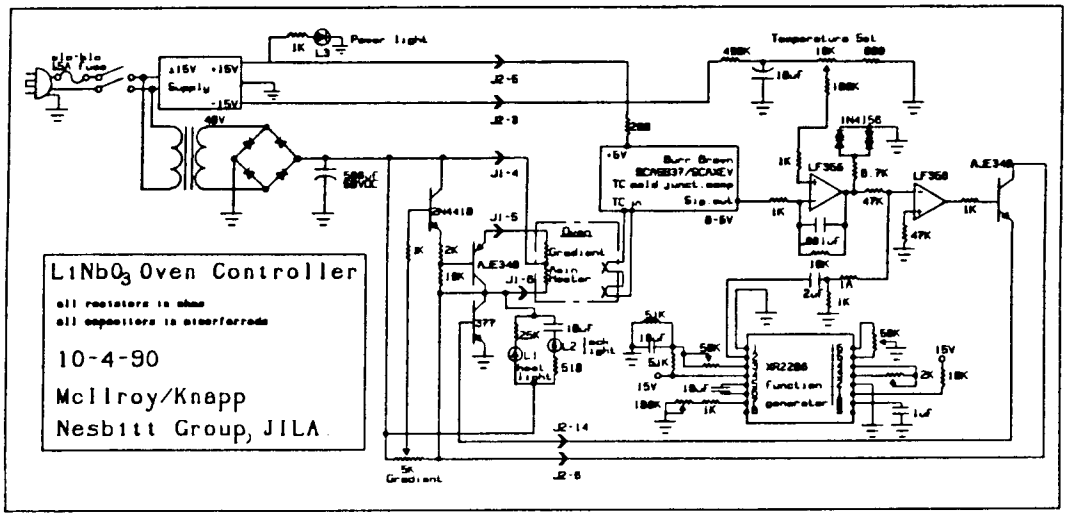

Figure 2.5 Circuit diagram for home built crystal oven temperature controller.

difference frequency generation of 2.2-4.2 μm light in $LiNbO_3$ as a function of crystal temperature and IR wavelength for both the 488 nm and 514 nm argon ion laser transitions. The difference frequency IR light generated consists typically of 2-5 μW near 3000 cm^{-1} as measured with an InSb detector (80% quantum efficiency). The frequency noise is <4 MHz (<1.3×10^{-4} cm^{-1}) rms as measured by scanning over the sub-Doppler, 35 MHz full width at half maximum, FWHM, profile of the Q(1) line for the ν_3 v=1←0 transition of methane in a slit jet expansion and measuring the amplitude noise on the side of the transition. The scanning of the IR light is accomplished by synchronously scanning the cavity to which the dye laser is locked and the oven temperature to maintain the proper phase matching condition. The voltages which drive the reference cavity and oven are generated by a 12 bit digital to analog converter (D/A) controlled by the scan control program running on an AT class personal computer. With this method, scans of up to 1 cm^{-1} are routinely made with 4096 sequential 8 MHz steps. Longer scans of up to 3 cm^{-1} can be made by increasing the laser step size. The number of steps in a scan is limited by the 12 bit resolution of the D/A. Clearly, this limitation could easily be overcome with the 16 bit D/A's which have recently become commonly available.

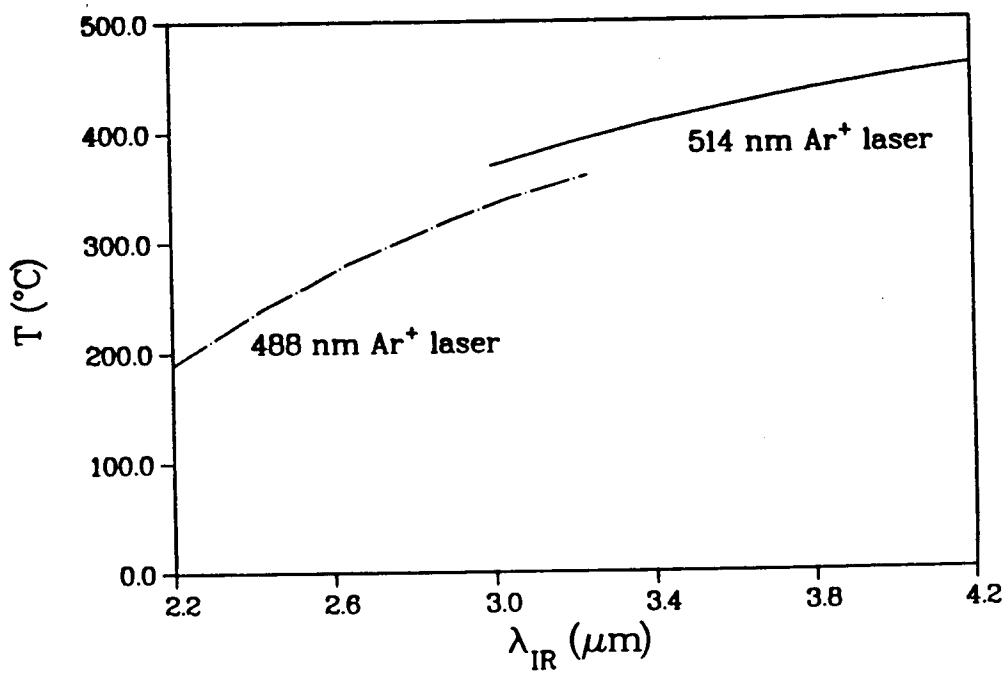

Figure 2.6 Temperature phase matching curves for difference frequency generation of 2.2-4.2 μm radiation in $LiNbO_3$ as a function of IR wavelength generated. Type I 90° phase matching is assumed. An R6G dye laser and Ar ion laser are used to generate the difference frequency.

Difference Frequency Generation of 1.2-2.2 μm Radiation

We wish to extend the frequency coverage of our spectrometer to include the region of the first overtones of hydrogen stretches, roughly 1-2 μm. The relatively low phase matching temperatures (<180 °C)[7] required to subtract the dye laser from the Ar ion laser in $LiNbO_3$ at short wavelengths, <2.2 μm, preclude the self annealing which, at higher temperatures, repairs index damage to the crystal due to partial absorption of the Ar ion laser light. This is the origin of the short wavelength cutoff for the dye/argon laser mixing. To reach below 2.2 μm by nonlinear subtraction, there are several possible solutions. A new nonlinear material may be found which does not have these problems. Alternatively, $LiNbO_3$ may be used with a new combination of lasers which can be phased matched at higher temperatures or which avoids laser wavelengths absorbed by the crystal.

Though a different material might seem the simplest solution, the problem is more difficult than it may first appear. $LiNbO_3$ does not have an especially large effective nonlinear index (d_{eff}= 1.5×10^{-8} cgs)[3], but it does possess an important characteristic for 90° phase matching over a wide range of frequencies: The n_e and n_o tune rapidly and at significantly different rates with temperature. Thus a wide range of phase matching conditions can be obtained simply by tuning the crystal

temperature. This combination of properties makes it desirable to retain $LiNbO_3$ as the nonlinear medium.

Since this temperature tuning technology is well developed for $LiNbO_3$, a new combination of lasers is sought which can be phased matched in $LiNbO_3$. For operational simplicity, only a combination of a fixed frequency and tunable laser are considered. Certainly the most familiar, easily used, and widely tunable laser source is the visible dye laser lasing on a rhodamine dye (R6G). Others dyes and the recent development of the Ti:sapphire laser provide further options for the tunable laser. Ideally a single frequency laser would be available to take advantage of these well developed technologies to produce 1-2 μm radiation by difference frequency mixing.

Happily, a simple solution exists; a Nd:YAG laser at 1.064 μm can be subtracted from a visible dye laser to obtain the desired frequencies. The phase matching temperatures are predicted from the temperature dependent Sellmeier equation of Edwards and Lawrence[5] for $LiNbO_3$ indices of refraction n,

$$n^2 = A_1 + \frac{A_2 + B_1 F}{\lambda^2 - (A_3 + B_2 F)^2} + B_3 F - A_4 \lambda^2 \qquad (2.6)$$

where A_1, A_2, A_3, A_4, B_1, B_2, and B_3 are constants listed in Table 2.1 and λ is the vacuum wavelength in microns. F contains the temperature dependence and is given by

Table 2.1: Coefficients of the temperature dependent Sellmeier equation for $LiNbO_3$ (Equ. 2.6).[a]

	ordinary axis	extraordinary axis
A_1	4.9048	4.5820
A_2	0.11775	0.09921
A_3	0.21802	0.21090
A_4	0.027153	0.02194
B_1	2.2314×10^{-8}	5.2716×10^{-8}
B_2	-2.9671×10^{-8}	-4.9143×10^{-8}
B_3	2.1429×10^{-8}	2.2971×10^{-7}

[a]See Ref. 5.

$$F=(T-T_o)(T+T_o+546) \qquad (2.7)$$

where T_o=24.5 C. Predictions of the phase matching temperature using Eq. 2.6 show that difference frequency mixing of the dye and Nd:YAG lasers to produce 1.2-2.2 μm radiation can be achieved with essentially the same temperature range (150-500 °C) used to generate the 2.2-4.2 μm radiation (see Fig. 2.7). Thus the same oven and crystal can be used for tuning between 1.2-4.2 μm. Since the dye laser is ω_1 and the Nd:YAG laser is ω_2 (see Eq. 2.1), the dye laser must be polarized along the optic axis of the crystal, just as the Ar ion laser is for the generation of 2.2-4.2 μm light.

For the difference frequency production of 1.2-2.2 μm light, we employ a 300 mW, diode pumped, monolithic, solid state Nd:YAG laser (Lightwave Electronics, Model 122-1064-300F) with specified line width of <5 kHz over 1 ms, <50 MHz/hr long term drift and <0.1% amplitude noise. The temperature stabilized, solid state ring resonator design clearly requires no additional stabilization since its short term stability is inherently 3 orders of magnitude better than the dye laser described above. To combine the dye and Nd:YAG beams, a polarization beam splitter coated to reflect the 1.06 μm light is used as previously described for the Ar ion laser in the 2.2-4.2 μm mixing. A bandpass filter is again used to separate the difference frequency light

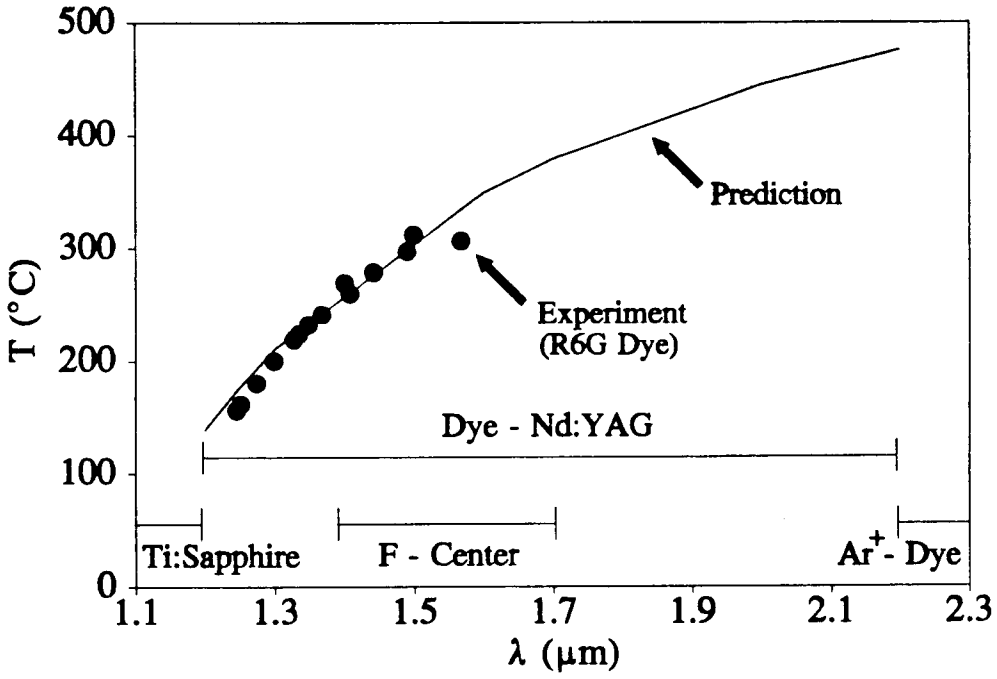

Figure 2.6 Temperature phase matching curves for difference frequency generation of 1.2-2.2 μm radiation in $LiNbO_3$ as a function of IR wavelength generated. Type I 90° phase matching is assumed. The solid line is the curve predicted from the temperature dependent Sellmeir equation. The • represent experimental points measured with an R6G dye laser and Nd:YAG laser to generate the difference frequency. The experimental points are limited by the tuning range of the R6G dye. At the bottom, the frequency coverage of other common cw lasers in this region are shown.

from the far more intense pump lasers.

Fig. 2.7 shows excellent agreement between the phase matching curve predicted from the temperature dependent Sellmeier equation and that measured with our apparatus for the difference frequency generation of 1.2-2.2 μm light in $LiNbO_3$. For these measurements, a 5 mm thick Si flat is used to filter out the visible laser and much of the Nd:YAG laser before detection with a 0.25 mm^2 intrinsic Ge detector. To discriminate against the Nd:YAG light which makes it to the detector, the dye laser is chopped. The range of phase matching temperatures which could be experimentally accessed is limited by the R6G dye currently used in the dye laser. With a redder dye such as DCM or a Ti:sapphire laser the entire tuning range should be easily realized.

Throughout the tuning range, the difference frequency power is predicted to increase quadratically with IR frequency ω_3.[9] Fig. 2.8 shows the difference frequency power as a function of IR wavelength, normalized to dye laser power and Ge detector response. The unexpected drop in IR power at short wavelength (high frequency) may be due to index damage caused by a combination of low phase matching temperatures (<200 C) and short dye laser wavelength (<585 nm). At 1.3 μm, with ~300 mW of dye laser and ~300 mW of Nd:YAG laser power, the difference frequency power is measured to be

~5 μW assuming a Ge detector quantum efficiency of 60%.

To demonstrate the utility of this 1.2-2.2 μm laser source, the HF stretching overtone spectrum ($20^0 \leftarrow 00^0 0$) of ArHF is recorded with the experimental arrangement shown in Fig. 2.9. This arrangement is essentially identical to that used for the 2.2-4.2 μm studies with the substitution of the Nd:YAG laser for the Ar ion laser and Ge detectors for InSb detectors. The slit jet and signal detection scheme is described later in this Chapter. Fig. 2.10 shows the ArHF HF stretching overtone spectrum between P(15)-R(14). The signal to noise achieved on this weakly bound complex suggests that many such overtone experiments are possible, and indeed the HF stretch overtone bands in $(HF)_2$ have also been identified. The analysis of these spectra will appear in separate publications.

Slit Jet Expansion and Gas Handling System

Slit Jet Expansion

The slit free jet expansion[10-16] provides a source of rotationally, vibrationally and translationally cooled molecules in conjunction with a long optical pathlength and narrow linewidths. The mechanics of our pulsed slit valve have been described in detail elsewhere.[15,17] Typically the 4 cm × 57 μm slit valve is open for 500 μs with a repetition rate of 19 Hz to avoid synchronous 60

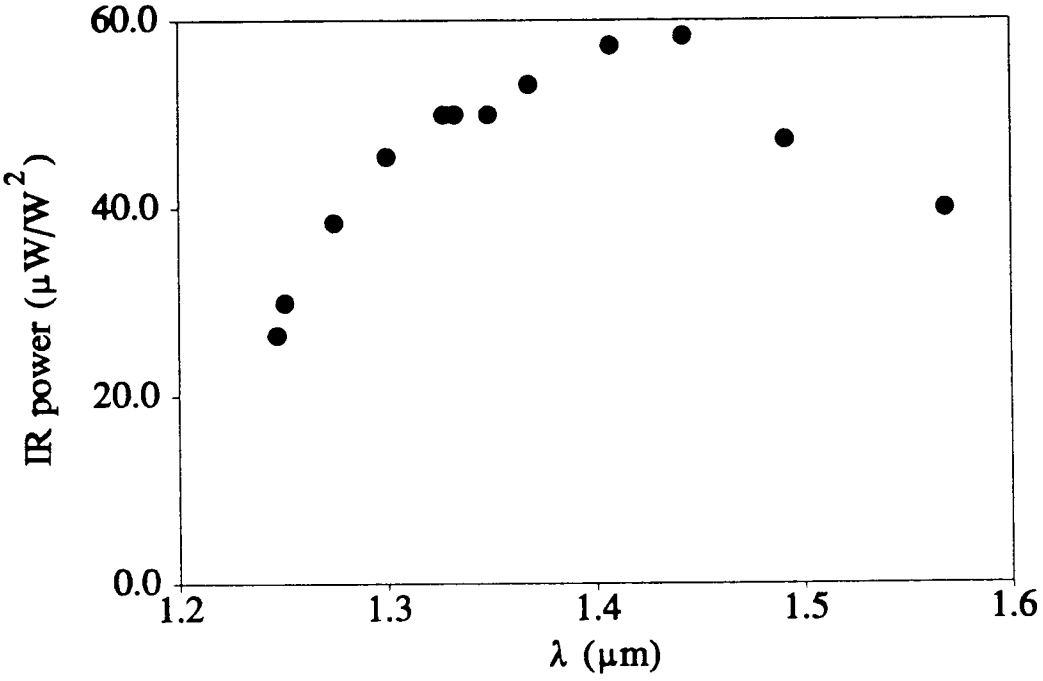

Figure 2.8 Power versus wavelength curve for the generation of difference frequency light with an R6G dye laser and Nd:YAG laser. The difference frequency power is in μW of IR per W of dye laser per W of Nd:YAG laser. The curve is normalized to Ge detector response. At 1.3 μm, with ~300 mW of dye laser and ~300 mW of Nd:YAG laser power, the difference frequency power is measured to be ~5 μW assuming a Ge detector quantum efficiency of 60%.

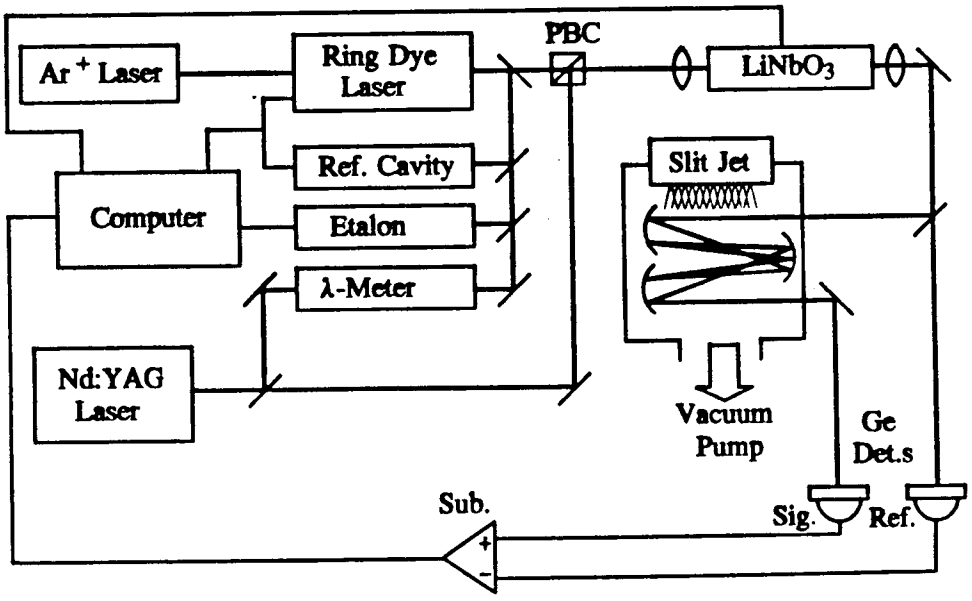

Figure 2.9 Slit jet, difference frequency IR laser spectrometer for 1.2-2.2 μm studies. PBC is a polarization beam splitter used to combine the orthogonally polarized dye and Ar ion lasers.

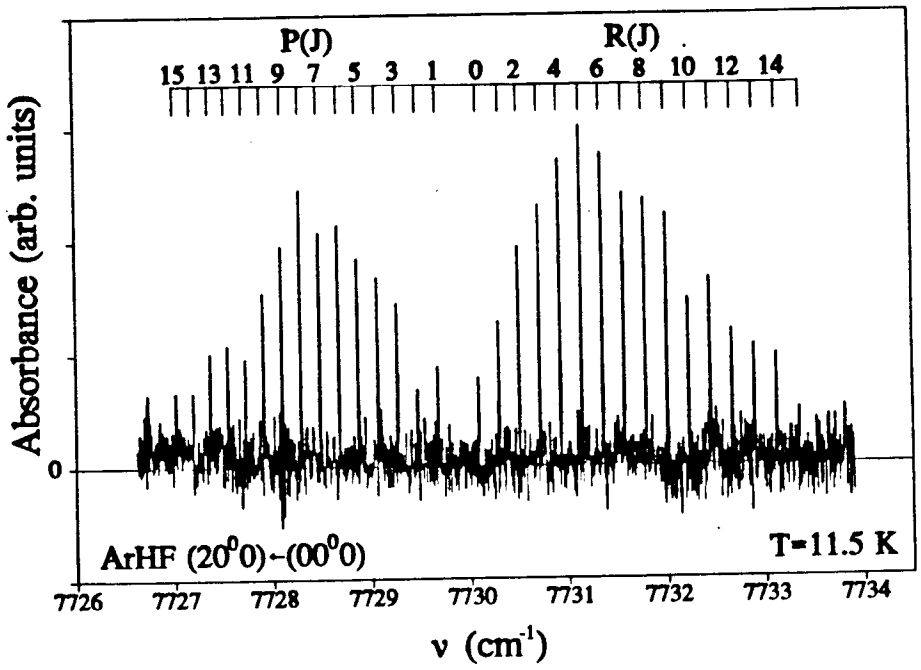

Figure 2.10 ArHF HF stretching overtone $(20^0 0) \leftarrow (00^0 0)$ spectrum recorded with slit jet, difference frequency IR laser spectrometer. The difference frequency light is generated by mixing of a single frequency ring dye laser and a single frequency ring Nd:YAG laser.

Hz noise. Gas is removed from the vacuum chamber by the combination of a rotary pump and a blower booster pump which have a combined pumping speed of 540 ℓ/s. Even with this pumping speed, the high flux levels of the slit nozzle result in a steady state vacuum chamber pressure of 120 mTorr with a backing pressure of 1000 Torr of He. This relatively high background pressure is acceptable because the high gas density of the slit expansion prevents the formation of the shock wave (i.e. Mach disk) before the wall of the vacuum chamber; in the absence of wall effects, the Mach disk is predicted[14] to form approximately one meter downstream at this background pressure. The valve is mounted on an X-Y translation stage within the vacuum chamber. This allows the valve to be centered over the laser beam and the downstream distance of the probe to be adjusted to ±0.06 cm from typically x=0.5-1.0 cm, allowing studies of cooling and clustering as a function of position in the jet.

To facilitate the interpretation of spectra complicated by additional transitions due to intramolecular vibrational mixing, it is important to know if the slit expansion can be described by a rotational and vibrational temperature. If this is possible, then the number of rotational and vibrational states populated can easily be predicted along with their expected intensity distribution with standard Boltzmann

statistics. Deviations from Boltzmann statistics would then be the first indications of state mixing in the molecule. Unequilibrated J and K state distributions have been observed in pinhole expansions of, for example, NH_3.[16] However, in our slit jet, we have never observed similar disequilibration in J or K rotational state populations. For example, the Boltzmann plot of the propyne ν_2 transitions in Fig. 2.11 is linear, with all J states populated in the jet falling on the same line described by T_{rot}=4.5 K, indicating excellent rotational equilibration. For highly symmetric molecules such as propyne (C_{3v}), the K state cooling is limited by nuclear spin symmetry considerations, which are discussed later in this Section.

Vibrational equilibration is more difficult to assess due to signal to noise ratio (S/N) limitations. For example, if the vibrational temperature is the same as the rotational temperature, the population of v=1 of the lowest frequency vibration of any hydrocarbon discussed here (skeletal torsion of 1-pentyne, ~100 cm^{-1}) would be 10^{-16} of the ground state population at T=4 K, making detection of hot bands impossible. No transitions arising from vibrationally excited states of propyne (lowest vibrational frequency 328 cm^{-1}, see Chap. III) are observed, which is consistent with $T_{vib} \leq 70$ K given the signal to noise ratio limit of this experiment.

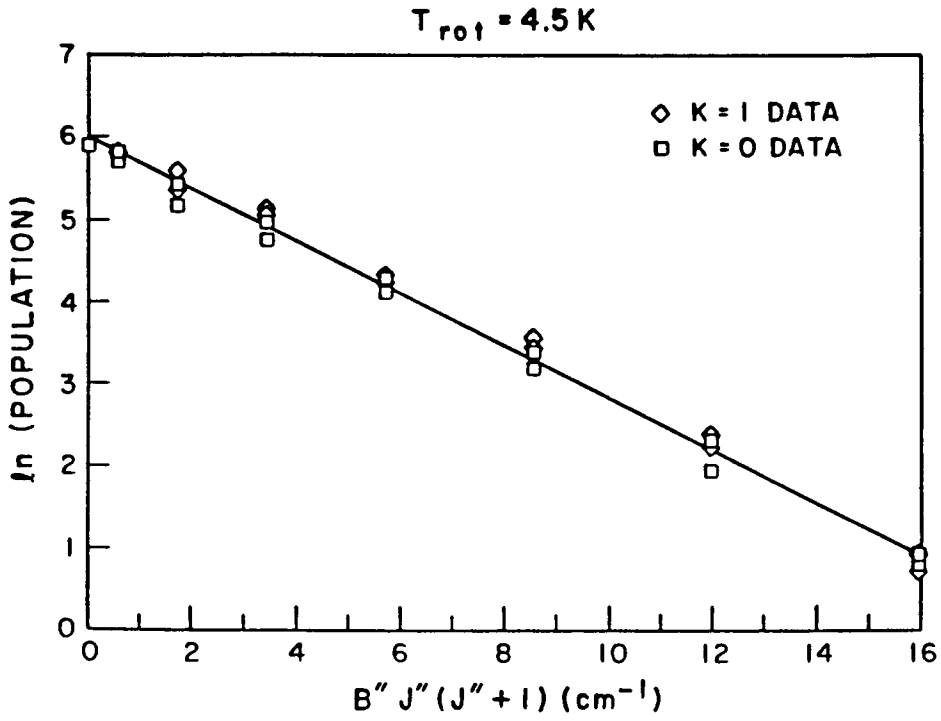

Figure 2.11 Boltzmann plot of all observed propyne ν_2 rovibrational transitions. Note the linearity for all J indicating excellent equilibration of rotational states populated in the slit jet.

Furthermore, for HF-OCO, hot bands of the extremely low frequency (~10 cm^{-1}) bend states show excellent vibration-rotation equilibration.[18] The greater equilibration in the slit than in the pinhole may be due to two reasons: 1) the factor of two greater number of hard sphere collisions than in a pinhole expansion and 2) the long range, low velocity collisions that occur later in the expansion when the gas density in a slit jet is still relatively high compared to a pinhole expansion.[17]

Nuclear spin state populations and symmetries also affect the intensity of transitions, and thus it is important to check whether nuclear spin states relax in a predominantly rare gas slit expansion. With four equivalent hydrogens (nuclear spin 1/2) in a highly symmetric tetrahedral arrangement, methane provides a good test of this behavior. At a typical jet rotational temperature of 4 K, only J=0 would be significantly populated in the absence of nuclear spin, but if spins do not relax, symmetry considerations predict that J=0,1,2 are populated in ratios of 5:9:2 even at T=0 K. The spectrum then consists of the allowed transitions from these states with intensities predicted by statistical weights and Hönl-London factors. In Table 2.1, experimental intensity ratios measured in a He expansion are compared to these predictions with agreement to within a root mean square deviation of 1.2%, indicating

that spin relaxation is not an important process in rare gas slit expansions. Propyne and many other hydrocarbons containing three or more identical hydrogens show nuclear spin limited cooling similar to that observed in methane.

Jet Diagnostics

For the studies of intramolecular vibrational coupling, other diagnostics and precautions are also used to assure that the molecular beam is composed almost solely of monomeric species. Two principal diagnostics are commonly used to verify the composition of the molecular beam. First, when the laser is tuned to a monomer absorption, the shape of the transient absorption from the slit valve gas pulse is monitored. In the absence of clustering, the absorption appears as approximately a square pulse in time as the gas flow is turned on (50 μs rise time), held on briefly (~500 μs), and then turned off (~50 μs fall time). If the concentration of absorbers or the total pressure are increased to the point that cluster formation begins, a dip appears in the center of the time domain absorption profile (see inset of Fig. 2.12). A dip appears rather than a constant loss of absorption intensity, since the valve pulse is not homogeneous in time. During the opening of the valve a pressure gradient develops across the orifice so that the molecules that the laser encounters appear to come from a lower pressure expansion

Table 2.2: CH_4 intensity ratios at T = 4 K.[a]

Intensity Ratio	Experiment	Predicted
P(1):P(2)	2.50	2.50
Q(1):Q(2)	4.62	4.50
R(0):R(1)	1.00	1.00
R(1):R(2)	5.34	5.36
R(0):R(2)	5.37	5.36

[a]From direct absorption measurements in a slit jet expansion with 1.0% CH_4 in 1000 torr He.

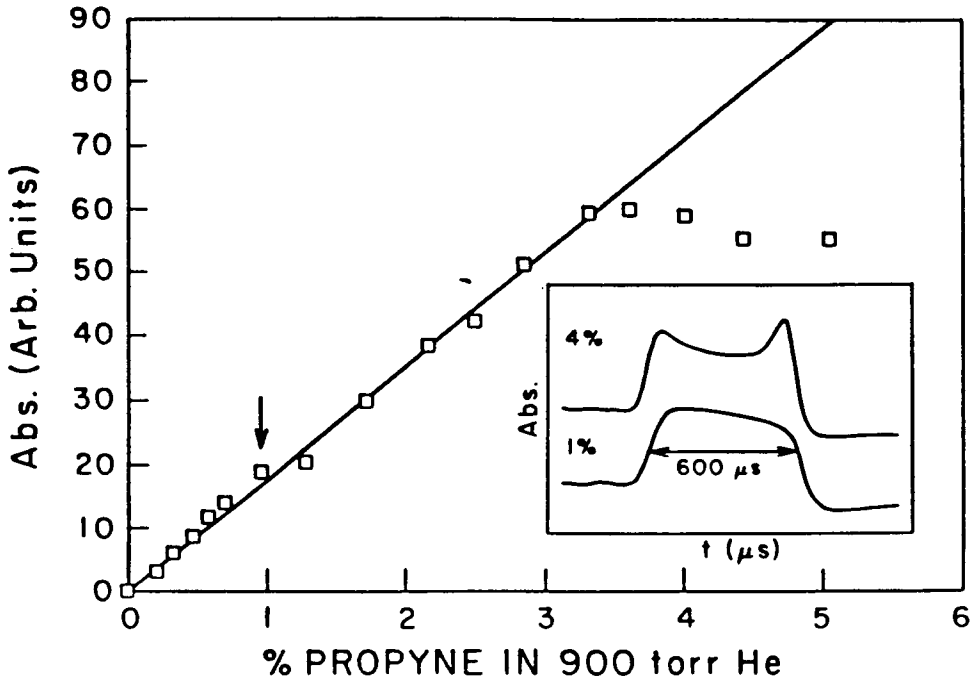

Figure 2.12 Clustering diagnostics. The main plot shows the growth of propyne absorbance in a slit jet as a function of propyne concentration in He. The backing pressure is 1000 torr. Note the loss of linear growth at ~4% propyne in the expansion. This occurs at the same concentration that a dip in the slit jet pulse absorption is first observed (see insert). The loss of linear growth and dip in absorption pulse are both characteristic of clustering.

with less clustering. As the valve becomes fully open, the gradient dies away and clustering reduces the concentration of monomer species in the expansion causing a decrease in monomer absorption. The closing of the valve briefly reestablishes the gradient giving a final increase in absorption. Since a lower pressure expansion also produces less cooling, it is important not to monitor absorption on a high J line populated only at warmer temperatures. Such states can produce similar absorption profiles because population is transferred to lower J's as the expansion cools. This technique typically detects clustering after ~5% of the reagent molecules are lost.

A second, more sensitive diagnostic also depends on the loss of monomer absorption as clusters form. Again the laser is tuned to a monomer absorption. However, rather than visually monitor the pulse shape, the entire pulse is integrated with baseline correction as described below. By varying the concentration of reagent in the beam and plotting the change in absorption, the onset of clustering can be detected as the point where the increase in absorption with reagent becomes nonlinear. A sample plot for propyne in 1000 torr He is shown in Fig. 2.12. Note that the plot is very linear up to ~4% absorber concentration. This behavior is typical of all hydrocarbons investigated to

date.

Using the diagnostics described above, dilute He expansions (~1% reagent) are found to produce no detectable clusters. Thus, He is used as the carrier gas in all the hydrocarbon IVR experiments. This minimization of clustering is expected for two principal reasons. First, He is very light (atomic mass of 4 amu) and thus has a greater propensity for elastic collisions. Though this reduces its cooling efficiency, it also makes it more difficult for it to act as a third body to stabilize the formation of a cluster. Second, He has a very low polarizability (8 times less than Ar)[19], and thus the forces that hold van der Waals clusters together, multipole-induced multipole and induced multipole-induced multipole interactions, are very weak. Indeed even with extreme expansion conditions (2000 torr He) and despite the large molecular dipole and quadrapole moments of HF and HCl, it has proven difficult to make detectable quantities of even He-HF and He-HCl, though the spectra of these van der Waals molecules have now been recorded.[20] Thus, He expansions are preferred to minimize cluster formation.

Gas Handling System

A schematic of the gas handling system is shown in Fig. 2.13. Gas mixtures may be prepared for expansion from the slit valve in two general ways: gases may be

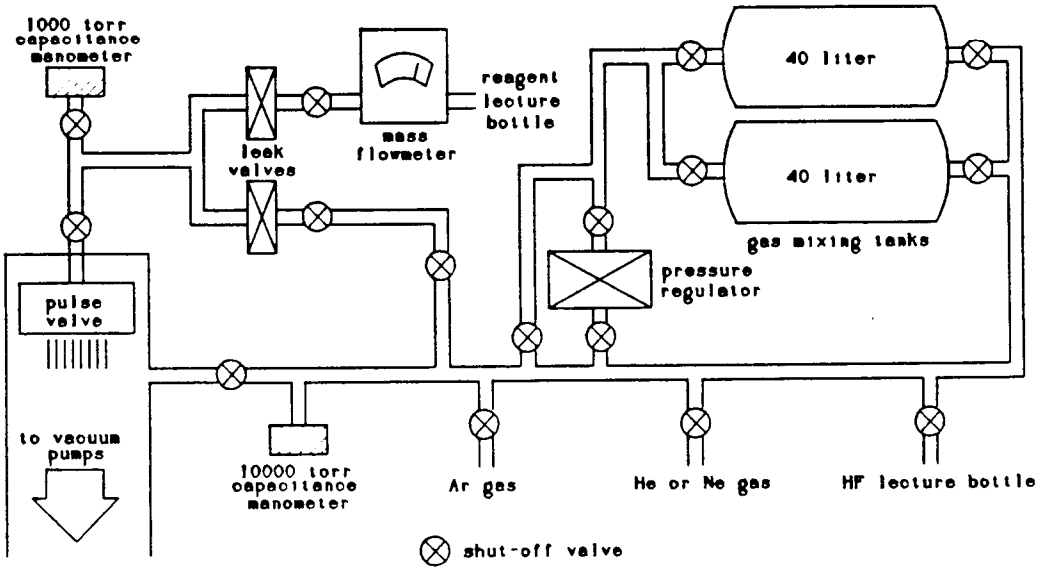

Figure 2.13 Gas Handling system for slit jet spectrometer.

premixed in a reservoir or they may be continuously mixed together as they flow to the slit valve. Some common mixtures have also been purchased premixed in large commercial high pressure (~100,000 torr) cylinders, but these were not used in the experiments described in this dissertation. A home made "premix" is prepared in one of the two mixing tanks; capacitance manometers are used to measure the partial pressure of each component as it is added. The components are added in order of increasing concentration for two reasons. First, this makes the measurement of small partial pressures easier since we are not trying to measure a small difference in a large number. Second, by adding the highest concentration (usually >95%) component last, high flow rates into the tank can be used to induce turbulent mixing of the gases. The mixture is then allowed to mix diffusively for >1 hr to insure a homogeneous composition.

The tanks used for home made premixes are limited to only ~2500 torr total pressure by safety constraints. When flowing gas from these tanks, a regulator (Matheson Model 3602) is used to set slit valve backing pressures that are above atmospheric pressure. To achieve backing pressures below atmospheric pressure, the regulator is set to about 800 torr and a variable leak valve (Granville-Phillips Model 203) is used to constrict flow to the slit valve. The backing pressure is measured by a

capacitance manometer immediately behind the slit valve. For mixtures that are primarily Ar, these reservoir premixes provide enough gas for several hours of running with backing pressures below 500 torr and a 19 Hz repetition rate. However, the hydrocarbon spectra require mixes of primarily He and higher backing pressures, ~1000 torr. Since for the same backing pressure, He flow rates are >3 times higher than for Ar,[17] premixing in the reservoirs proves impractical; a single fill lasts for less than <1 hr, time for only 2-3 full scans.

For the He based mixtures, a second approach is used relying on continuous, "on the fly" mixing of the He and reagent gases. To achieve this, the He carrier and reagent absorber gas flows are combined immediately before the slit valve. These flows are controlled by separate leak valves as shown in Fig. 2.13. The total backing pressure is monitored with a capacitance manometer after the flows are combined. Since only very dilute (~1% reagent) mixes are made this way, the total backing pressure is a good approximation for the carrier gas partial pressure. The small concentration of reagent is monitored with a mass flowmeter (Tylan Model FM 380) immediately before the reagent control leak valve. If a premixed gas is substituted for the He or reagent, this same method may be used to create three or more component

mixtures. This type of mixing is more thoroughly described in Chap. VII since it is used in the synthesis of the Ar_nHF clusters.

Absorption Detection and Signal Acquisition System

The transient absorption of the difference frequency laser light is detected by a combination of long absorption path length, amplitude noise subtraction, and gated detection. The union of these three features gives this apparatus excellent sensitivity, 10^{-6} abs./$Hz^{1/2}$ or ~10^{-4} abs. in the instrument's usual 5 kHz bandwidth (BW). For reference, a diagram showing the major electrical connections in the spectrometer is shown in Fig. 2.14.

Signal Detection and Amplitude Noise Subtraction

The IR light is split into signal and reference beams of approximately equal intensity, of which only the signal beam passes through the expansion. The signal beam is multipassed through the slit expansion to increase the absorption pathlength. To minimize Doppler broadening and thus obtain the highest resolution, a double pass arrangement is used giving a total absorption pathlength of 8 cm. The IR light passes through the jet parallel to the long dimension of the slit, and then is nearly retro reflected (<1° reflection angle) off a flat gold mirror back to the detector. Alternately, for

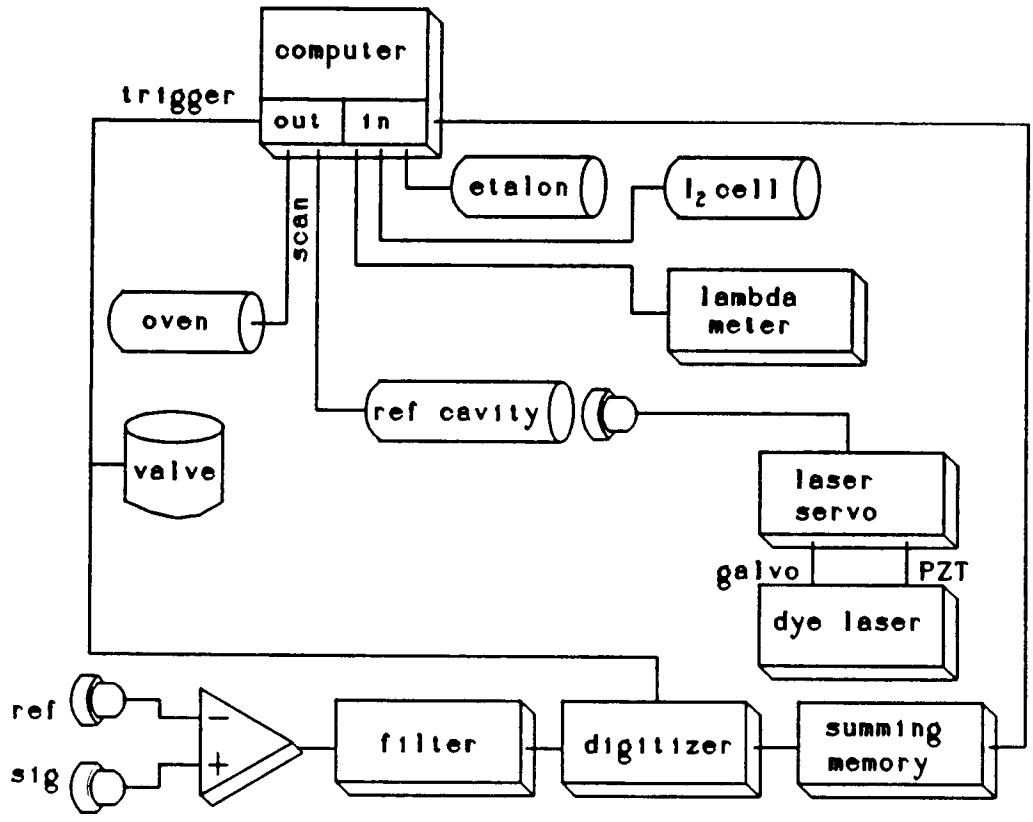

Figure 2.14 Schematic of major electrical connections in the slit jet, difference frequency IR spectrometer.

higher sensitivity, a 12 pass White cell (30 cm radius of curvature gold mirrors) is used giving a total pathlength of 48 cm. All passes are in the plane of the slit expansion. Though this multipass configuration has a longer pathlength, it suffers from two problems. First, a larger portion of the jet is sampled by the IR light, ~1 cm (~150 slit widths) from the first to last pass. Thus regions of different temperature or cluster size may be sampled. Second, in the White cell, the beams pass through the expansion at steeper angles, increasing the Doppler broadening observed in the expansion from 35 MHz FWHM in the double pass configuration to 65 MHz FWHM in the 12 pass configuration as measured for ν_6 (~3100 cm^{-1}) of cyclopropane (1% in 1000 torr He).

The signal and reference beams are focussed on to one of a matched pair of 77 K InSb detectors (Santa Barbara Research Model 40742) with dc coupled transimpedance amplifiers for the 2-4 μm experiments or room temperature intrinsic Ge detectors (EG&G Judson Model J16-18A-500U) for the 1-2 μm experiments. The noise characteristics of the InSb detectors used in the experiments discussed here are discussed in Ref. 17. The two signals are then subtracted in one of two differential amplifiers. Early experiments employed a Tektronix 7A18 preamplifier in a Model 7704A oscilloscope with a common mode rejection ratio (CMRR) of 250 in the

10 Hz to 10kHz bandwidth (BW) used in the experiment. The bandwidth limiting, bandpass filter was of a passive, single pole design placed after the subtracting preamplifier.

Later, a dedicated subtraction preamplifier was constructed and remains in use. The circuit diagram for this differential amplifier is shown in Fig. 2.15. It largely mimics the function the Tektronix preamplifier with several improvements. A Burr-Brown differential amplifier (Model INA105, CMRR=10000, 1 MHz BW) is used for subtraction. Matched passive circuit elements are used in the input stages to achieve a minimum CMRR of 250 in the experimental 10 kHz BW. Signal/reference balancing is achieved by using a combination of a discrete, variable attenuator on the signal input and a continuously variable attenuator on the reference input. A second potentiometer at the reference input serves to vary the input impedance and is found experimentally to be necessary to obtain the highest possible CMRR. This variable input resistance probably produces a phase shift. A discrete attenuator is used on the signal input so that overall signal gain is reproducible on a day-to-day basis. After the Burr-Brown amplifier, three output signals are available. The first follows immediately after the variable amplifier (BW 300 kHz), the second follows an active 2 pole low pass filter at 10

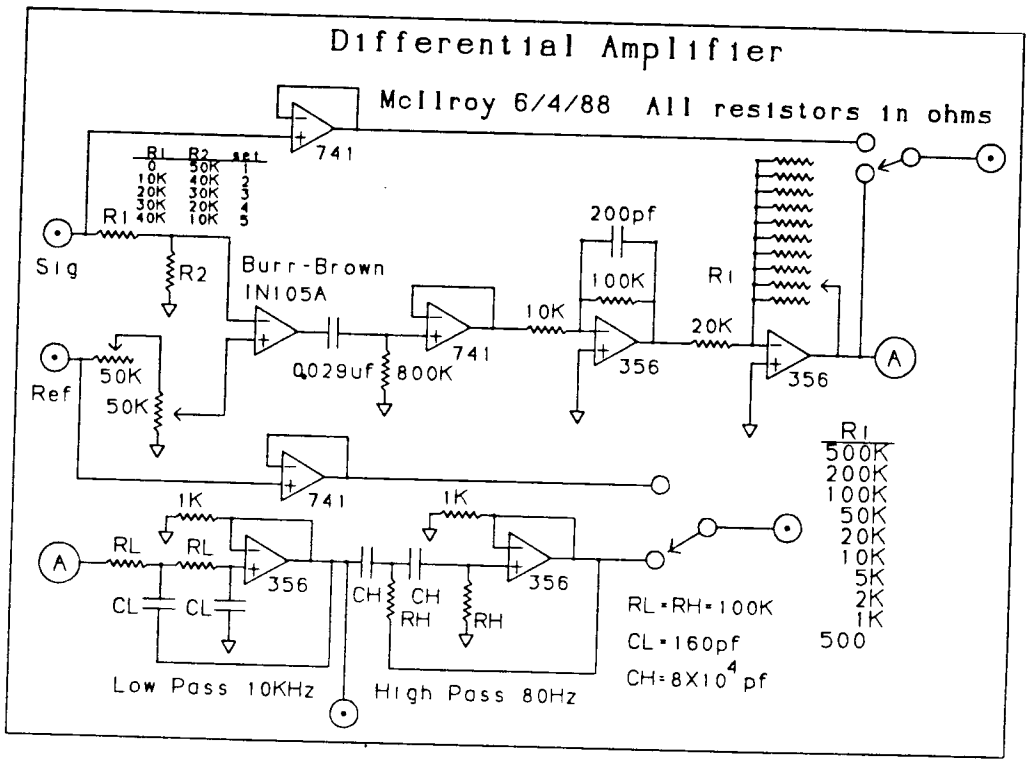

Figure 2.15 Circuit diagram for differential amplifier used to subtract signal and reference outputs.

kHz, and the third follows an additional active 2 pole high pass filter at 80 Hz. The first output is used solely for diagnostic purposes during set up of the experiment. The second output with only low pass filtering is for use with the transient digitizer/signal averager data acquisition system. The third bandpass output is for realtime monitoring of the signals during data acquisition; the additional filtering makes signal detection easier.

Digitization and Integration of Signal

After subtraction and low pass filtering, 2000 μs of signal surrounding the ~600 μs long time dependent absorption is digitized by an 8 bit transient recorder (DSP Model 2001S, 1 μs/point) contained in a CAMAC crate (DSP Model Optima 860). For signal averaging, the digitizer is hardwired to a dedicated 24 bit summing memory (DSP Model 4100) also contained in the crate. The summing memory is capable of working at up to 100 Hz repetition rates. The number of averages and other control statements are sent by the instrument control computer through the CAMAC interface (DSP Model 6001). Fig. 2.16 displays a sample digitized signal. When the averaging is complete, three gates, pre-signal (256 μs), signal (512 μs), and post-signal (256 μs), are transferred to a single integer array in the computer through a dedicated high speed, parallel CAMAC interface,

making use of the direct memory access mode of the computer. The positions in time of these three gates are adjustable via the instrument control program. These three gates allow for exact correction of errors due to time domain baseline offset and slope and should be equally spaced in time.

An assembly code subroutine (listed in Appendix I) then integrates the three gates in real time. The pre-and post- gates are subtracted from the signal to remove any offset or slope in the time trace providing a flat baseline for the detection of weak, spectrally broad absorbance. In Fig. 2.17, a model signal with integration gates marked is shown with offset, b, and slope, m, errors of the form mt+b. Integration of the first baseline gate gives

$$\int_{t_1}^{t_2} gate_1\, dt = \frac{1}{2} m(2t_1 d + d^2) + bd \qquad (2.8)$$

the second signal gate gives

$$\int_{t_3}^{t_4} gate_2\, dt = \frac{1}{2} m(4t_1 d + 8d^2 + 4dD) + 2bd + signal \qquad (2.9)$$

and the third baseline gate gives

$$\int_{t_5}^{t_6} gate_3\, dt = \frac{1}{2} m(2t_1 + 7d^2 + 4dD) + bd \qquad (2.10)$$

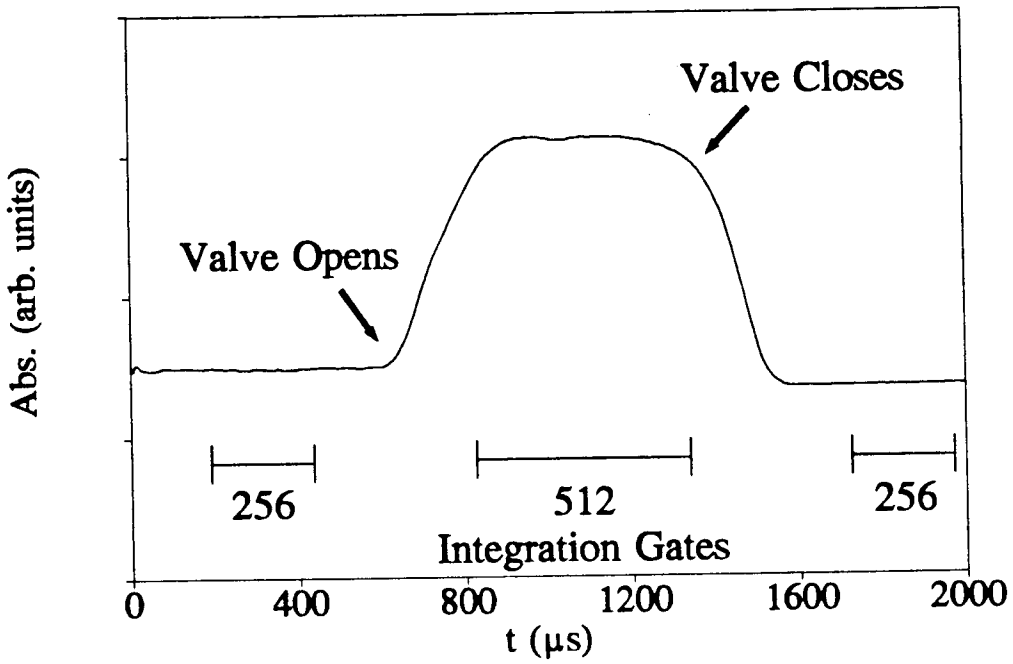

Figure 2.16 Sample digitized signal pulse showing positioning of integration gates.

The sum of these three then is

$$-\int_{t_1}^{t_2} gate_1\,dt+\int_{t_3}^{t_4} gate_2\,dt-\int_{t_5}^{t_6} gate_3\,dt=signal. \qquad (2.11)$$

leaving only the signal. Higher order corrections could be made by adding additional gates; however, these have not been found necessary. This ability to avoid spurious absorption baseline drift is important since strong rovibrational coupling can fragment a transition into so many closely spaced lines that an apparently continuous absorption may result. With twelve passes through the expansion, the system has a sensitivity of 2×10^8 molecules/cm^3/quantum state for the ν_3 CH stretch in methane which has an integrated absorption of 266 cm^{-2} atm^{-1}.[21]

Additional Diagnostics

In addition to the transient IR absorption in the expansion, several other quantities are monitored by the computer which controls the experiment. About 1% of the dye laser is sent to an air spaced, flat-flat, 95% reflecting quartz etalon (0.01075 cm^{-1} FSR, finesse 10), which provides a frequency scale for the spectrum, and to an I_2 fluorescence cell, which provides a unique fingerprint with which to overlap contiguous scans. The I_2 cell is generally necessary only for spectra which exhibit continuous absorption and lack an inherent

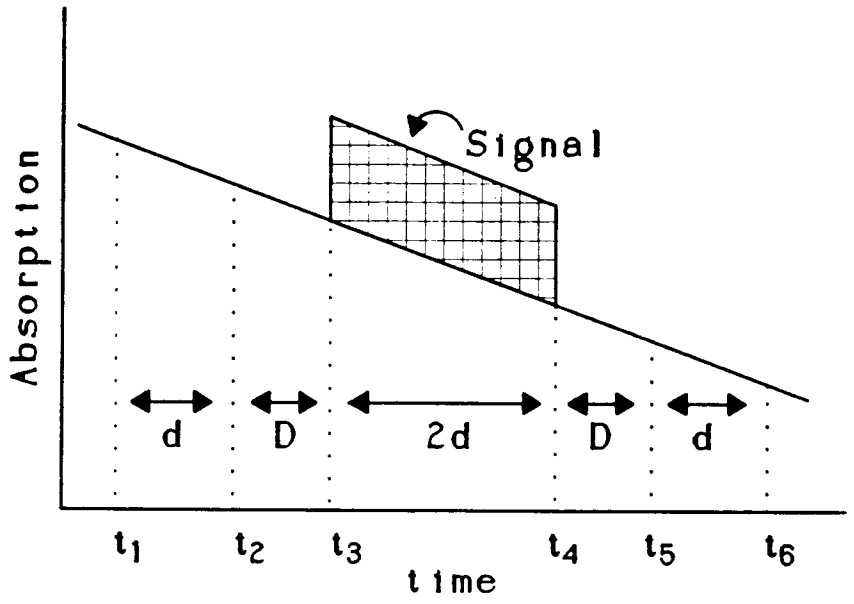

Figure 2.17 Model signal with slope and offset errors. The baseline integration gates are of length d and the signal gate of length 2d. D is the delay between the signal and baseline integration gates.

fingerprint. The etalon and I_2 cell signals are recorded at each laser step after filtering with a 10 Hz low pass filter. The IR power is also recorded every 10 laser steps for later normalization of the signal.

Wavelength Calibration and Data Analysis Methods

For accurate, absolute measurement of line positions, a travelling interferometer of the Hall and Lee design[22] (lambda meter) is used to measure the argon ion or Nd:YAG and dye laser frequencies simultaneously. A brief description is given here; see Ref. 17 for a detailed discussion of lambda meter use in the difference frequency system. Fig. 2.18 shows a schematic of the interferometer. The translating cart Doppler shifts the frequency of the lasers in one arm of the interferometer by $+\Delta\nu$ and in the other by $-\Delta\nu$. To first order this Doppler shift is given by

$$\Delta\nu = \frac{\nu_{laser} v_{cart}}{c} \qquad (2.12)$$

where ν_{laser} is the laser frequency, v_{cart} is the speed of the cart, and c is the speed of light. When the beams of each laser are recombined on their respective nonlinear photodiode detectors, a beat note signal is produced at $2\Delta\nu$ in the same way that the difference frequency of the dye and Ar ion lasers is produced in the nonlinear crystal. Clearly from Eq. 2.10, the frequency of the

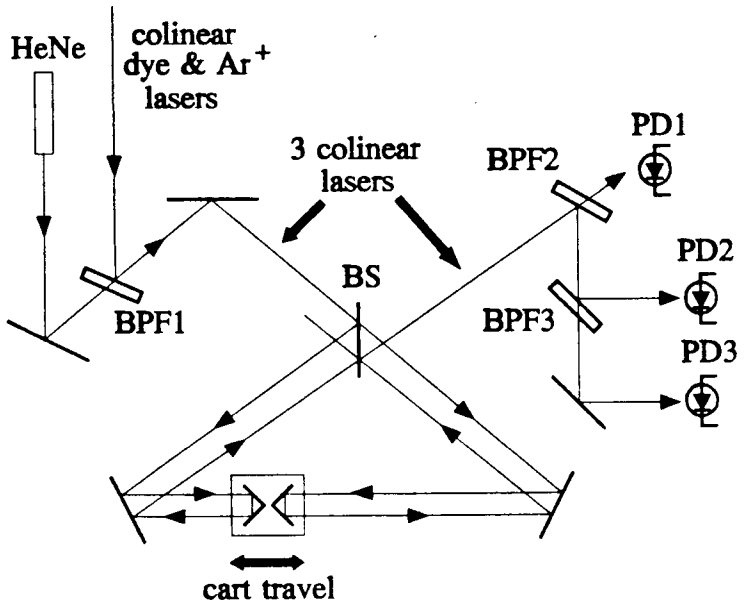

Figure 2.18 Schematic of the lambda meter.

beat note depends on the cart speed and the frequency of the laser. If the cart speed were known with great accuracy (to ~1 part in 10^8), the beat note frequency would be a direct measurement of the laser frequency. However, this is not practically possible. Instead we measure the ratio of the beat note frequency $\Delta\nu_{laser}$ of a laser whose frequency ν_{laser} is unknown relative to that of the HeNe laser $\Delta\nu_{HeNe}$ whose frequency ν_{HeNe} is known

$$\frac{\Delta\nu_{laser}}{\Delta\nu_{HeNe}} = \frac{\frac{\nu_{laser}V_{cart}}{C}}{\frac{\nu_{HeNe}V_{cart}}{C}} = \frac{\nu_{laser}}{\nu_{HeNe}} \qquad (2.13)$$

thus eliminating the need to measure v_{cart}.

The dye laser, Ar ion or Nd:YAG laser, and a polarization stabilized HeNe laser are inserted simultaneously into the lambda meter. Upon exiting the interferometer, the beams are separated by a series of interference filters. Interference fringes produced by translating the corner cubes on the linear air bearing are detected by recombining the beams from the two arms of the interferometer on a fast (1 MHz BW) photodiode detector (Si photodiode for the visible lasers and Ge for the near IR Nd:YAG laser). The photodiode beat note signals are each passed through a discriminator to produce TTL level square waves at the fringe frequency of each laser.

To measure the relative beat note frequencies,

the zero crossings of the HeNe, dye and Ar ion (or Nd:YAG) laser fringes are digitally counted until a preset number of HeNe fringes is reached. This is equivalent to determining the ratio of the beat note frequencies. The number of HeNe fringes is chosen so that the number of fringes counted for the other lasers is equal to their frequency in wavenumbers. Since there is no integral relationship between the HeNe and other laser frequencies, the other lasers will generally be midway between zero crossings when the last HeNe fringe is counted. Missing this fractional fringe would limit the accuracy of this lambda meter to ~0.01 cm^{-1}. To minimize this counting error, the dye laser and Ar ion or Nd:YAG laser fringe frequencies are actually multiplied by 16 in a phase locked multiplier. Thus the fractional fringe lost when the last HeNe fringe is detected will be at most 1/16 of an actual fringe, and the frequency accuracy is extended to 0.001 cm^{-1} on a single reading. The HeNe fringe frequency is not increased by frequency multiplication since an integral number of fringes is counted by definition.

The frequencies of the Ar ion or Nd:YAG and dye lasers are then directly read from the display of the digital counter or stored in the instrumental control computer. To increase the precision of a frequency measurement, multiple readings (20-30 typically) of a

single transition are taken; these are then averaged in the computer to extend the measurement to a precision of 0.0003 cm^{-1}. Due to PZT creep in the lasers and reference cavities, manual adjustment of the dye laser is needed during the measurement process to keep the difference frequency tuned to the molecular absorption line center.

Though the frequency measurement method described up to this point produces very precise measurements (0.0003 cm^{-1}), the accuracy is relatively poor with typical errors of ~0.05 cm^{-1}. These errors arise from several sources. First, the pathlength through the interferometer is not exactly same for all three lasers. Indeed, since 0.001 cm^{-1} accuracy in the frequency measurement of the visible lasers requires having the same pathlength to a part in 10^8, small, milliradian differences in alignment cause significant errors. In addition to alignment errors, there are dispersion errors due to the fact that the measurement is made in air. These dispersion errors are large (~0.03 cm^{-1} typically for the Ar ion laser) and frequency dependent (~0.003 at typical dye laser frequencies of ~16000 cm^{-1}).[23] To correct for alignment and dispersion errors, an infrared reference transition is measured in the jet within 50 cm^{-1} of the transitions of interest and used to calculate an empirical correction term. The use of this correction term assumes that the jet conditions approximate a vacuum

and that the correction is approximately constant between the reference line and the line to be measured. This correction method has been shown to yield IR frequency accuracies of <0.0005 cm^{-1}.[17] For the hydrocarbon work, methane[24], ethane[25], and HCl[26] are used as frequency standards. For the Ar_nHF cluster work, HF[26] and ArHF[27] transitions are used. With this system, an absolute IR frequency accuracy of better than 0.0003 cm^{-1} is readily obtained.[1,17]

Although this system produces high accuracy frequency measurements, it is laborious to use. Furthermore, it is awkward to apply to clumps of closely spaced (<0.005 cm^{-1}) lines since it becomes difficult to know which transition the laser is tuned. Many closely spaced transitions in a single scan (~1 cm^{-1}) are the common situation in the hydrocarbon and Ar_nHF spectra. Thus it is desirable to minimize the number of line positions that are necessary to measure with the lambda meter, but still have a means of determining line positions and splittings to high accuracy. To this end, a computer program was developed to graphically display the spectrum, select peaks, and determine their frequencies by interpolating and extrapolating from peaks measured with the lambda meter. A frequency scale is obtained from the etalon fringes (FSR≈0.01075 cm^{-1}) recorded simultaneously with the spectrum. The program

exists in two versions, LAMCAL, for Hercules graphics based PC's, and LAMVGA, for VGA graphics based PC's. Both use the same frequency determination algorithm and a listing of LAMVGA is included in Appendix II.

The programs function as follows: A spectrum is loaded, and a peak finding algorithm is used to locate the etalon fringe channel numbers (laser steps) which are stored in an array. The peak finder uses a minimum peak size discriminator and looks for points which are higher (lower) than ±5 surrounding points. This gives the peak to the nearest integer channel number. To further refine the peak position, an analytic, 3 point parabolic approximation to the top of the peak is used. The highest (lowest) point and one at a user defined distance to either side are used to uniquely determine the parabolic coefficients. The peak position is then calculated from the zero derivative of the parabola. After the etalon peaks are found, the etalon is calibrated from two peaks in the scan whose frequencies are known from the literature or from lambda meter measurements. These two peaks should be near the beginning and end of the scan to maximize the number of etalon FSR's used in the calibration. A reference peak is then marked in the spectrum, and its frequency entered to provide an absolute reference for interpolation and extrapolation. To enter the peaks whose frequency is

desired, either the automatic peak finder may be used or the peaks may be located manually. Both options use the parabolic peak finder described above. The manual option is useful for scans with a rolling baseline or low signal to noise ratios in which the peak finder may mark many spurious peaks. The etalon peaks are then used to determine the peak positions which may be stored for later use and/or printed out.

This wavelength interpolation/extrapolation scheme could be significantly improved by the construction of a actively stabilized cavity locked to the HeNe reference laser. The etalon could then be calibrated once using two widely space reference absorptions, and only a single lambda meter measurement would be needed for each scan. Locking the fixed frequency Ar ion or Nd:YAG laser to this same cavity would further reduce frequency measurement errors.

These analysis programs also provide several other useful utilities. The spectrum may be smoothed using Pascal's triangle weighting. Intensity fluctuations due to changes in the IR power during a scan may be removed. These are significant since $I-I_o$ is recorded, not $\ln(I_o/I)$. The programs also allow for the removal of spurious "spikes" (very large, single channel aberrations) which occasionally appear in the spectra. A facility is also included for the conversion of the data

from the compact, binary encoded, intensity/channel number format in which it is stored to an ASCII intensity/wavenumber format which is more convenient for fitting line shapes and making figures. During this conversion the number of points in the spectrum may be reduced, effectively reducing the resolution, to facilitate plotting of an entire spectrum. This can be a significant problem since a single scan of ~1 cm^{-1} contains 4096 points, and a complete spectrum may be up to 30 cm^{-1} long which would requiring ~2 MB of computer memory. Since the laser printers usually used to plot of the data have a resolution of only 300 dots per inch or 3000 points across a typical spectrum, reducing the number of points in the scan for display purposes has little affect on the appearance while greatly speeding plotting and reducing storage requirements.

REFERENCES FOR CHAPTER II

1. C. M. Lovejoy and D. J. Nesbitt, J. Chem. Phys. **86** 3151 (1987).

2. Y.-R. Shen ed., Nonlinear Infrared Generation (Springer-Verlag, Berlin, 1977).

3. A. Yariv, Quantum Electronics (John Wiley and Sons, New York, 1975).

4. S. Yu. Volkov, D. N. Kozlov, P.V. Nikles, A. M. Prokhorov, V. V. Smirnov and S. M. Chuskin, Soviet J. of Quantum Electron. **11**, 135 (1981).

5. G. J. Edwards and M. Lawrence, Optical and Quant. Electron. **16**, 373 (1984).

6. D. F. Nelson and M. Mikulyak, J. of Applied Phys. **45**, 3688 (1974).

7. A. S. Pine, J. Opt. Soc. Am. **66**, 97, (1976).

8. S. Yu. Volkov, D. N. Kozlov, P. U. Nikles, A. M. Prokhorov, V. V. Smirnov, and S. M. Chuskin, Sov. J. Quantum Electron. **11**, 135 (1981).

9. Y.-R. Shen ed., Nonlinear Infrared Generation, (Springer-Verlag, Berlin, 1977) 29.

10. K. Veeken and J. Reuss, Appl. Phys. B **38**, 117 (1985).

11. A. Amirav, U. Even, and J. Jortner, Chem. Phys. Lett. **83**, 1 (1981); A. Amirav, U. Even, J. Jortner, F. W. Birss, and D. A. Ramsay, Can. J. Phys. **61**, 278 (1982).

12. M. Sulkes, C. Jouvet, and S. A. Rice, Chem. Phys. Lett. **87**, 515 (1982).

13. O. F. Hagena, Surface Science **106**, 102 (1981).

14. A. E. Beylich, Z. Flugwiss. Weltraumforsch. **3**, 48 (1979).

15. C. M. Lovejoy and D. J. Nesbitt, Rev. Sci. Instrum. **58**, 807 (1987).

16. D. L. Snavely, S. D. Colson, K. B. Wiberg, J. Chem. Phys. **74**, 6975 (1981).

17. C. M. Lovejoy, Doctoral Thesis (University of Colorado, Boulder, 1990) Chapt. II.

18. D. J. Nesbitt and C. M. Lovejoy, J. Chem. Phys. **93**, 77 (1990).

19. A. A. Radzig and B.M. Smirnov, Reference Data on Atoms, Molecules, and Ions (Springer-Verlag, Berlin, 1980).

20. C. M. Lovejoy and D. J. Nesbitt, J. Chem. Phys. **93**, 5387 (1990).

21. M. Dang-Nhu, A. S. Pine, and A. G. Robiette, J. Mol. Spectrosc. **77**, 57 (1979).

22. J. L. Hall and S. A. Lee, Appl. Phys. Lett. **29**, 367 (1976).

23. R. C. Weast, Ed. CRC Handbook of Chemistry and Physics (CRC Press, Boca Raton, 1989).

24. M. Dang-Nhu, A. S. Pine, and A. G. Robiette, J. Mol. Spectrosc. **77**, 57 (1979).

25. A. S. Pine and W. J. Lafferty, J. of Research of the N. B. S. **87**, 237 (1981).

26. G. Guelachvili, Opt. Commun. **19**, 150 (1976).

27. C. M. Lovejoy and D. J. Nesbitt, J. Chem. Phys. **91**, 2790 (1989).